



Two-dimensional amorphous heterostructures of Ag/a-WO_{3-x} for high-efficiency photocatalytic performance

Yumei Ren^{a,1}, Chong Li^{b,1}, Qun Xu^{a,*}, Jun Yan^c, Youzeng Li^a, Pengfei Yuan^b, Huicong Xia^a, Chunyao Niu^b, Xinan Yang^d, Yu Jia^{b,e,**}

^a College of Materials Science and Engineering, Zhengzhou University, Zhengzhou 450001, PR China

^b International Laboratory for Quantum Functional Materials of Henan, and School of Physics and Engineering, Zhengzhou University, Zhengzhou 450001, PR China

^c Liaoning Provincial Key Laboratory of Textile Cleaning, Dalian Polytechnic University, Dalian 116034, PR China

^d National Laboratory for Condensed Matter Physics and Institute of Physics, Chinese Academy of Sciences, Beijing 100190, PR China

^e Key Laboratory for Special Functional Materials of Ministry of Education, College of Advanced Materials Science, Henan University, Kaifeng 475004, PR China

ARTICLE INFO

Keywords:

2D Amorphous tungsten oxide
2D Amorphous heterostructures Ag/a-WO_{3-x}
Amorphous effect catalysis
d-d Tail states coupling
Synergistic photocatalysis

ABSTRACT

Synergistic photocatalysis is an important concept for designing the high-efficiency catalysis for fundamental research and technical applications. In this study a well-defined synergistic photocatalysis system is realized by the 2D amorphous heterostructures (2DAHs) Ag/a-WO_{3-x}, which are constructed by Ag nanoparticles on 2D amorphous tungsten oxide (a-WO_{3-x}) fabricated via supercritical CO₂ method. We demonstrate theoretically that the oxygen evolution reactions (OER), characterized by photocurrent response, have been dramatically improved in Ag/a-WO_{3-x} than those of both single a-WO_{3-x} and Ag/WO₃ systems. Such an enhanced photoelectrochemical performance attributes to the superposition effect of amorphous effect catalysis and local surface plasmon resonances (LSPR) catalysis. More interestingly, the *ab initio* density-functional theory calculations reveal that the amorphous effect catalysis ascribes to the unique *d-d* tail states coupling of both Ag and W atoms in the 2DAHs. Overall, our findings not only propose the prototype of synergistic photocatalysis, but also provide a new methodology to the design of novel catalyst.

1. Introduction

Atomically thin two-dimensional (2D) materials with unexpected optical, thermal, and electronic properties have been dramatically attracted with increasing interest in this decade [1–3]. And their corresponding heterostructures constructed by these 2D materials have provided an extensive platform for exploring the physics and fabricating various nanodevices [1,4,5]. Such 2D heterostructures, such as *h*-BN/graphene, WS₂/MoS₂, and as well as mixed-dimensional van der Waals (vdW) heterostructures [5,6–9], can efficiently integrate the properties of their isolated components with desirable properties for practical applications, including electronics, optoelectronics, catalysis, energy conversion and transfer, etc [6,10]. Nowadays the 2D crystalline heterostructures can be successfully fabricated by using various assembling techniques such as mechanical transfer, chemical vapor deposition (CVD) or physical epitaxy, and so on, and many fabricated nanodevices exhibit excellent properties, *i.e.*, light-emitting diodes,

photodetectors, photovoltaic cells, flexible and transparent devices and so on [1,10,11–13]. Compared with 2D crystalline heterostructures, 2D amorphous heterostructures (2DAHs) are not easy to be fabricated because the individual amorphous counterparts are relatively difficult to obtain, let alone the unavailability of aforementioned assembling techniques. Therefore, it is still a great challenge to find a proper way to fabricate the 2DAHs, which possess peculiar phenomena and potential applications.

As for low-dimensional (LD) amorphous structures, to date, most of them are limited in zero-dimensional (0D) and one-dimensional (1D) experimentally. For example, amorphous lithium-incorporated palladium phosphosulfide nanodots (Li-PPS NDs) [14], amorphous MoO_{3-x} nanoparticle [15], amorphous ZnO nanocages [16], amorphous Fe-CoPO_x nanowires [17], amorphous Co(OH)₂ nanorod [18], amorphous carbon nitride [19] as well as amorphous molybdenum sulfide [20,21], all of the experimental studies demonstrate that these amorphous nanostructures can exhibit superior activities, especially in the field of

* Corresponding author.

** Corresponding author at: College of Materials Science and Engineering, Zhengzhou University, Zhengzhou 450001, PR China.

E-mail addresses: qunxu@zzu.edu.cn (Q. Xu), jiayu@zzu.edu.cn (Y. Jia).

¹ These authors are the co-first authors.

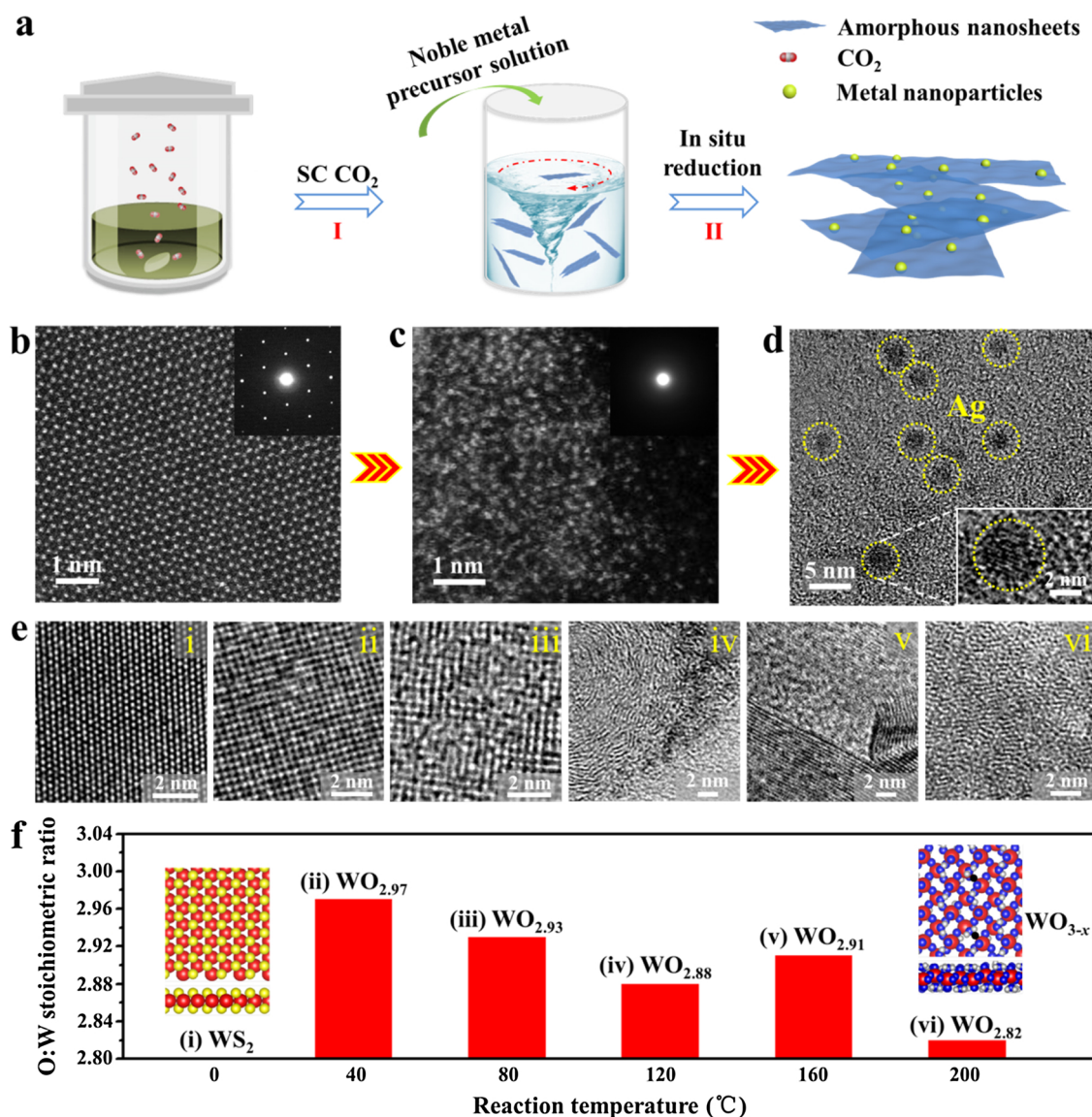


Fig. 1. a) Illustration of the experimental procedures for preparation of the metal/a-WO_{3-x} amorphous heterostructures that includes the following steps: i) the structure transforms from WS₂ nanosheets to amorphous WO_{3-x} nanosheets; ii) the metal/a-WO_{3-x} heterostructures synthesized by a solution-processed *in situ* reduction method. b) STEM-HAADF image of the exfoliated WS₂ nanosheets, and their corresponding SAED pattern is shown as inset. c) STEM-HAADF image of amorphous WO_{3-x} nanosheets with the corresponding SAED pattern. d) HRTEM images of Ag/a-WO_{3-x} heterostructures. e) TEM images of the structure transformation, (i) the exfoliated WS₂ nanosheets; (ii)-(vi) WS₂ nanosheets treated with assistance of SC CO₂. f) The corresponding chemical formula of the as-prepared products in (e).

catalysis and local surface plasmon resonances (LSPR). To our best knowledge, there have been no 2D ultrathin amorphous materials reported except our most recent work. Using the supercritical CO₂ (SC CO₂) technology, we successfully extend the 0D and 1D amorphous materials to 2D ones, namely amorphous MoO₃ nanosheets [22]. And we demonstrate that the 2D amorphous MoO₃ exhibits LSPR in the visible and near-IR regions, making it the candidate for designing high efficiency photocatalyst.

In this report, a well-defined 2D amorphous heterostructures, denoted as Ag/a-WO_{3-x}, can directly be constructed by dispersing Ag on few-layered amorphous tungsten oxide (a-WO_{3-x}). We theoretically demonstrate that the photocurrent response of Ag/a-WO_{3-x} can reach up to 2.6 and 1.7 times larger than those of a-WO_{3-x} and Ag/WO₃ systems, respectively. And the enhanced photoelectrochemical performance attributes to both amorphous effect and LSPR effect collectively. Furthermore, DFT calculations reveal that the amorphous effect is ascribed to the unique cooperative *d-d* tail states coupling mechanism of

Ag and W atoms in the 2DAHs. Based on these findings, we propose the concept of synergistic photocatalysis that serves as a new methodology for the design of high-efficiency catalyst.

2. Experimental

2.1. Materials

Commercially available WS₂ powder was purchased from Sigma Aldrich (Product Number: 243639). Commercially available WO₃ powder was purchased from Sigma Aldrich (Product Number: 95410). Ethanol used in all experiments was purchased from Sinopharm Chemical Reagent Co., Ltd. (China) and used without further purification since the reagent is of analytical grade. CO₂ with purity of 99.99% was provided by the Zhengzhou Shuangyang Gas Co. and it was used as received. Aqueous solution was prepared with double-distilled water.

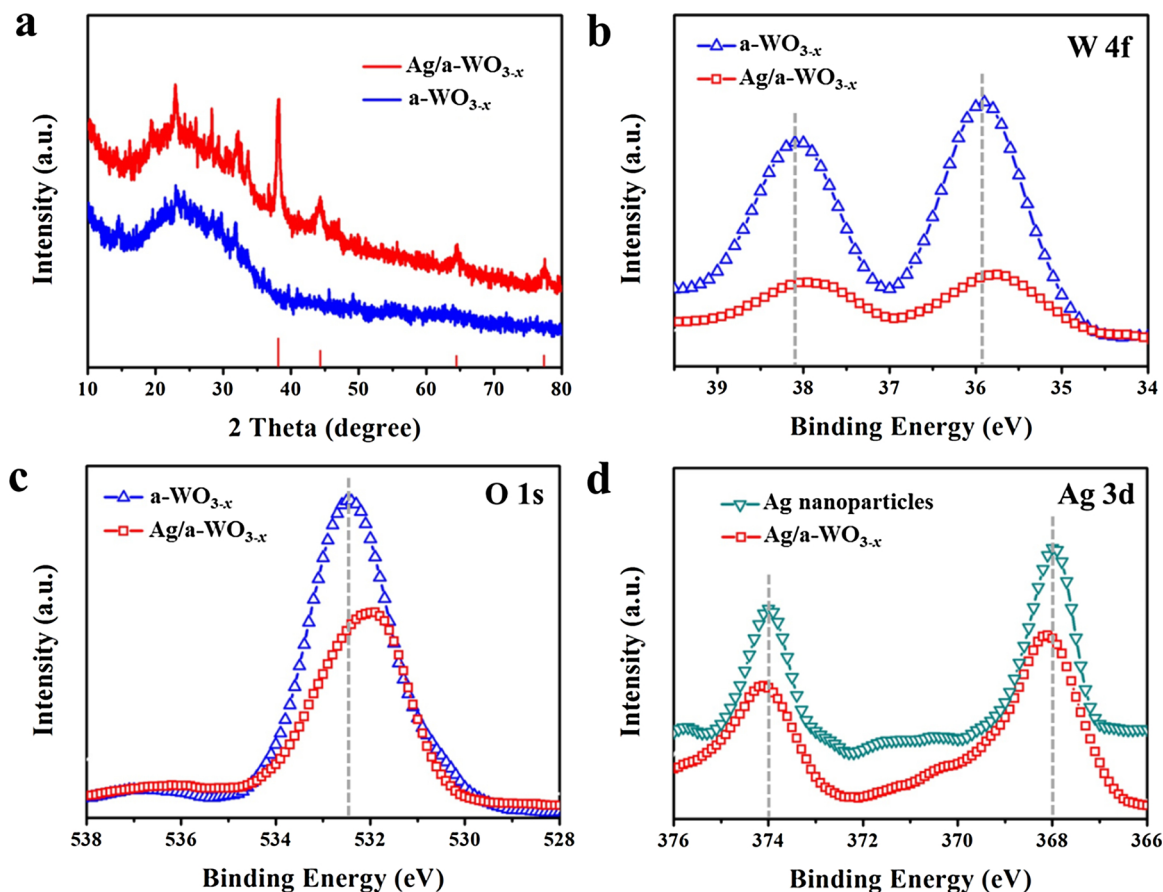


Fig. 2. a) XRD patterns of a-WO_{3-x} nanosheets and Ag/a-WO_{3-x} heterostructures, respectively. Deconvoluted high-resolution XPS of selected core energy level peak region: b) W 4f and c) O 1s XPS spectra of a-WO_{3-x} and Ag/a-WO_{3-x}. d) Deconvoluted high-resolution XPS of selected core energy level peak regions: Ag 3d for Ag nanoparticles and Ag/a-WO_{3-x}.

2.2. Liquid-exfoliation of bulk WS₂

Bulk WS₂ powder (50 mg, Sigma-Aldrich Reagent Inc.) was added to 100 mL flask. 10 mL of ethanol/water mixtures with ethanol volume fractions of 50% were added as dispersion solvents. The dispersion in the sealed flask was sonicated in the bath for 6 h, and then the dispersion was centrifuged at 5000 rpm for 30 min. to remove aggregates. The supernatant was collected by pipette.

2.3. Chemical reactions of the exfoliated WS₂ nanosheets

The supernatant was quickly added into the supercritical CO₂ (SC CO₂) apparatus composed mainly of a stainless steel autoclave (50 mL) with a heating jacket and a temperature controller. The autoclave was heated to 473.2 K, and CO₂ was then charged into the autoclave to the desired pressure under stirring. After a reaction time of 6 h, the gas was released. Finally, the dispersion was collected.

2.4. Synthesis of Ag/a-WO_{3-x} and Au/a-WO_{3-x} heterostructures

Briefly, pure Ag nanoparticles were produced by quickly addition of sodium citrate solution (45.6 mg) and AgNO₃ (6.8 mg) solution to a certain volume aqueous solution. The mixture was stirred vigorously at room temperature, following by addition of a certain amount of ascorbic acid solution (200 μL, 0.1 mM). And the reaction lasted for 1 h. Au nanoparticles were produced in the same way, while the difference is the amount of chloroauric acid (13.6 mg). Considering Ag and Au can be reduced under light irradiation, we controlled the synthesis condition under darkness.

The resulting Ag/a-WO_{3-x} and Au/a-WO_{3-x} heterostructures were prepared by a facile *in situ* redox at room temperature. The metal loading was 3% by weight with respect to the semiconductor. The contrast sample Ag/WO₃ and Au/WO₃ composites were achieved in the same manner, where the WO₃ nanosheets were exfoliated from the bulk WO₃.

2.5. Characterization

The morphology and structure of the materials was characterized by transmission electron microscopy (TEM) (JEM-2100) and tapping-mode AFM (Nanoscope IIIA). The high-angle annular dark-field (HAADF) low-resolution scanning electron Microscopy (STEM) images and elemental mapping were taken using FEI Tecnai G2 F20 S-TWIN operating at 200 kV. X-ray diffraction (XRD) patterns of samples were measured on a Y-2000 X-ray Diffractometer with copper Kα radiation (λ = 1.5406 Å) operating at 40 kV and 40 mA. X-ray photoelectron spectroscopy was performed using a Thermo ESCALAB 280 system with Al/K (photon energy = 1486.6 eV) anode mono X-ray source. The electron paramagnetic resonance spectroscopy (EPR) was carried out using an Endor spectrometer (JEOL ES-ED3X) at room temperature. UV-vis spectra (Shimadzu UV-240/PC) were measured to evaluate the dispersions concentration.

2.6. Photoelectrochemical (PEC) measurements

The PEC measurements were taken using an electrochemical workstation (CHI660E) with a typical three-electrode cell. The as-prepared sample was used as the working electrode, a Ag/AgCl electrode and Pt

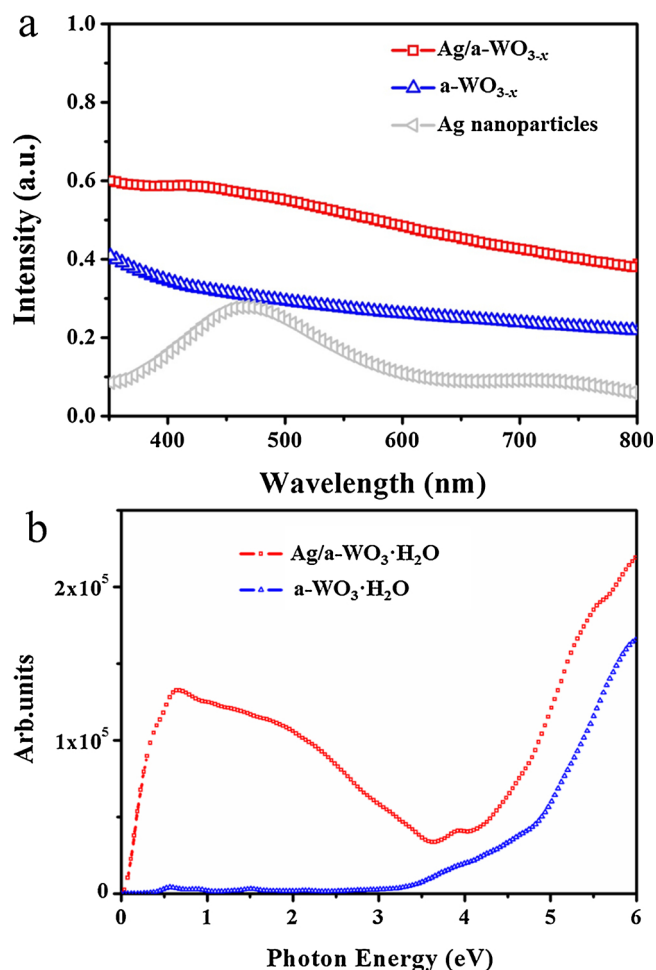


Fig. 3. a) Absorption spectra of Ag/a-WO_{3-x}, a-WO_{3-x} and Ag nanoparticles. b) The imaginary part ϵ_2 of the dielectric function for Ag/a-WO₃·H₂O and a-WO₃·H₂O.

wire were used as reference and counter electrode, respectively. Na₂SO₄ (0.5 mol L⁻¹) was used as the electrolyte. The working electrodes were prepared by dropping the suspension onto the surface of a clean fluorine-doped tin oxide (FTO) conductive glass substrate. The light ON-OFF switches were set as 100 s when measuring the I-t curves of the absolute values under visible light. The bias for the measurement was set as 0.8 V. The reversible hydrogen potential can be converted from the Ag/AgCl reference electrode potential as $E_{\text{RHE}} = E_{\text{vs Ag/AgCl}} + E_{\text{Ag/AgCl}}^0 + 0.059 \times \text{pH}$, where $E_{\text{Ag/AgCl}}^0$ is 0.1976 V at 25 °C.

The incident photon-to-current conversion efficiency (IPCE) spectra was collected by a solar simulator (Newport 66984, USA) coupled with a filter (Newport 71260) and an aligned monochromator (Newport 1-800-222-6440). All the electrochemical measurements were carried out by an electrochemical workstation (CHI 660E, Chen Hua Instrument, China). IPCE can be expressed by the equation: $\text{IPCE} = (1240 \times I) / (\lambda \times J_{\text{light}})$, where I (mA cm⁻²) is the measured photocurrent density at a specific wavelength, λ (nm) is the wavelength of incident light, and J_{light} (mW cm⁻²) is the measured irradiance at a specific wavelength.

2.7. Computational details

All the first-principles density functional theory calculations of the electronic properties were performed using the Heyd-Scuseria-Ernzerhof (HSE06) hybrid functional [23] as implemented in the Vienna *Ab initio* Simulation Package [24]. The interactions between electrons and cores were treated by the projector-augmented-wave method [25]. The cutoff energy of the plane-wave basis was set at

400 eV. The $2 \times 2 \times 1$ Monkhorst-Pack k-point meshes were used for Brillouin zone integration. The internal structures were fully relaxed until the Hellman-Feynman forces on all atoms were less than 0.02 eV Å⁻¹.

For the optical properties, the interaction between photons and electrons can be described by the frequency-dependent dielectric function $\epsilon(\omega) = \epsilon_1(\omega) + i\epsilon_2(\omega)$, where $\epsilon_2(\omega)$ can be calculated as

$$\epsilon_2(\omega) = \frac{4\pi^2 e^2 \hbar}{m^2 \omega^2} \sum_{ij} \frac{2}{(2\pi)^3} \int_{\text{BZ}} dk |M_{ij}(k)|^2 \delta[\omega - \omega_{ij}(k)]$$

The integral is over all states in the Brillouin zone. Matrix element is denoted as $M_{ij} = \langle \varphi_j(k) | e \cdot p | \varphi_i(k) \rangle$, here e and p are the polarization vector and the moment operator, respectively.

The calculated lattice constant of monolayer WO₃·H₂O is 5.12 Å and it agrees well with previous reported value [26]. For the simulation of a-WO₃·H₂O, we use a $4 \times 4 \times 1$ supercell with a certain concentration of O vacancy (including single and double O vacancies). Here it is worthwhile to stress that this size (> 2 nm) is large enough as a substrate that is covered by Ag or Au sub-monolayer. Then a molecular dynamic (MD) simulation was performed on this system up to 2 ps, and we randomly choose a snap as amorphous model without any structural relaxation. In our systems the H₂O molecular were added in WO₃ to stabilize the geometric structure, apparently it does not affect our potential physical mechanism for the reason that during the MD some H₂O molecules will desorb from WO₃ even in 300 K.

Then we study the vacancy-tolerant in terms of its formation energy E_f

$E_f = E_{\text{amo}} - E_{\text{cry}} + n \times 1/2 E(\text{O}_2)$ where E_{amo} and E_{cry} are the energies of Ag/a-WO₃·H₂O and Ag/c-WO₃·H₂O (here c refers to crystalline), respectively. $E(\text{O}_2)$ is the energy of the O₂. Fig. S1 clearly shows that when the concentration of O vacancy exceeds 2%, the E_f will increase sharply. It means that in the formation of Ag/a-WO₃·H₂O in experiment, it is facilitated when the concentration of O vacancy is at low range < 2%.

3. Results and discussion

3.1. Fabrication and morphology of 2DAHs of Ag/a-WO_{3-x}

The fabrication processes of the Ag/a-WO_{3-x} heterostructures are schematically described in Fig. 1a. First, monolayer and/or few-layer WS₂ nanosheets are exfoliated from bulk WS₂ with the assistance of SC CO₂ [27,28]. The exfoliated atomically thin WS₂ nanosheets can be easily oxidized in high-pressure CO₂ system leading to a lot of vacancies on the surface of the oxides [26,29–31]. Moreover, the diffusive atomic disordering can be achieved deriving from the straining force because of the strong interaction between CO₂ molecules and defects [22]. Then stable flaky amorphous phase of WO_{3-x} (a-WO_{3-x}) is successfully fabricated. Subsequently, the Ag/a-WO_{3-x} heterostructures are synthesized *in situ* reduction method, and the detail experimental process is in the methods section.

As shown in Fig. 1b, the corresponding selected-area electron diffraction (SAED) pattern indicates the hexagonal lattice structure of the exfoliated WS₂ nanosheets [32]. It is fascinating to find the completely disordered structure in 2D nanosheets of WO_{3-x} after treatment of SC CO₂ (Fig. 1c), and the low-magnification TEM images of the as-prepared a-WO_{3-x} nanosheets are presented in Fig. S2. The XPS results in Fig. S3 show that WS₂ nanosheets have been completely oxidized to tungsten oxide. TEM images in Fig. 1e display the structure transformation process from ordered to disordered structure with the variation of experimental temperature in SC CO₂, and their corresponding XRD results are supplied in Fig. S4. It can be known that the degree of oxidation of the exfoliated WS₂ nanosheets increased gradually with the increasing of oxidation temperature, and when the reaction temperature is over 120 °C, the WS₂ nanosheets are completely oxidized to WO₃.

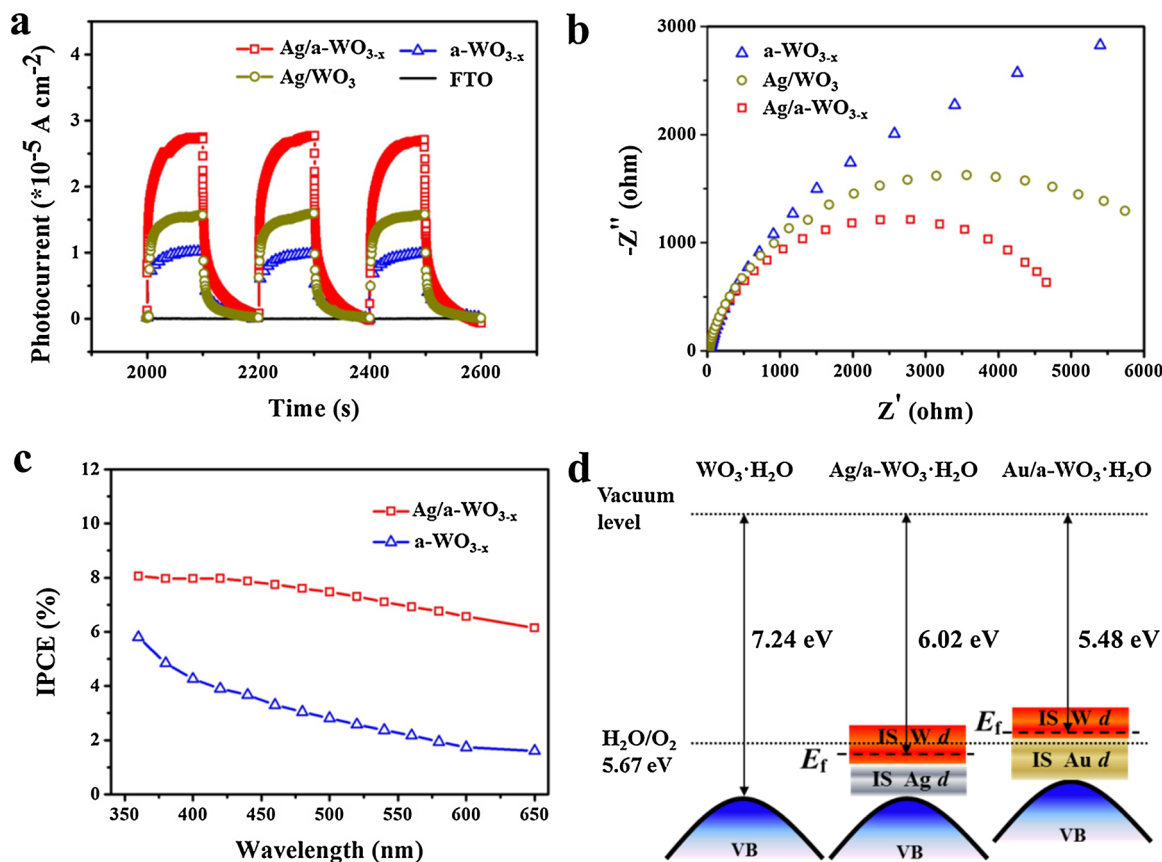


Fig. 4. a) The photocurrent response (0.8 V bias) of bare FTO glass, a-WO_{3-x}, Ag/a-WO_{3-x} and Ag/WO₃ coated FTO electrodes in 0.5 M Na₂SO₄ under simulated solar light illumination. b) EIS plots of a-WO_{3-x}, Ag/a-WO_{3-x} and Ag/WO₃ electrode in 0.5 M Na₂SO₄ illuminated by simulated solar light. c) IPCE spectra of a-WO_{3-x} and Ag/a-WO_{3-x} heterostructures measured at 0.8 V vs. Ag/AgCl. d) Schematically shows band alignments referring to the redox potential of water oxidation for oxygen generation in crystalline WO₃·H₂O, Ag/a-WO₃·H₂O and Au/a-WO₃·H₂O, respectively. The broad and narrow red bars represent relatively delocalized and localized interface state (IS) W-d state, respectively. The grey and yellow bars represent IS Ag and Au d band, respectively. All the calculated energies are aligned with vacuum level. (For interpretation of the references to colour in this figure legend, the reader is referred to the web version of this article).

What's more, the defect degree also increases along with the rise of temperature except for the reaction temperature of 160 °C, which has been reported in our previous work [31]. Combination of the two experimental characterizations, it can be judged that we can obtain the amorphous structure of WO_{3-x} at 200 °C in SC CO₂. Further their corresponding average oxygen vacancy percentages are listed in Fig. 1f, where the oxygen vacancy concentration can reach a maximum value, $x_{\text{max}} = 0.18$, at 200 °C in SC CO₂. Here, to further confirm the existence of oxygen vacancies in the as-prepared samples, electron paramagnetic resonance spectroscopy (EPR) spectroscopy was employed, which could provide sensitive and direct structural information. All the SC CO₂ treated samples exhibit an ESR signal at $g = 2.003$ (Fig. S5), which can be attributed to the existence of oxygen vacancies [33]. The signal intensity demonstrates that the WS₂-200 (that is a-WO_{3-x}) possesses the highest oxygen vacancies concentration among the five samples, which agrees well with the XPS results. Moreover, atomic force microscopy (AFM) measurement, a powerful method for precisely identifying the layer number, was performed to investigate the thickness of the nanosheets. As can be seen in Fig. S6, the thickness of the obtained a-WO_{3-x} nanosheets ranges from 2.6 to 3.5 nm, indicating that they exist as few-layer nanosheets in dispersions. And their average lateral dimension is about 150 nm.

Fig. 1d shows the HRTEM image of 2DAHs of Ag/a-WO_{3-x}, and it can be observed that the size of Ag nanoparticles is smaller than 5 nm and they are homogeneously embedded in the a-WO_{3-x} nanosheets. For a comparison study, the corresponding crystalline WO₃ as a matrix was performed as the control experiment. It can be found out that hardly any metal nanoparticles can dope in the WO₃ nanosheets, and the metal

nanoparticles are basically loaded on the edge of the WO₃ nanosheets (see Fig. S7).

3.2. Structure analysis and properties of 2DAHs Ag/a-WO_{3-x}

For the x-ray diffraction (XRD) patterns of Ag/a-WO_{3-x} heterostructures, the typical characteristic diffraction peaks of the Ag nanoparticles are indexed to face centered cubic structure Ag on a-WO_{3-x} (JCPD card No. 65-2871) (Fig. 2a) [34]. Beside this, with respect to a-WO_{3-x}, there are a little weak diffraction peaks probably because of the *in situ* redox reaction of the weakly reductive sub-stoichiometric WO_{3-x} with oxidative Ag precursors [35,36]. Owing to the oxygen vacancies, the as-prepared a-WO_{3-x} nanosheets can provide the necessary reduction potential. The X-ray photoelectron spectroscopy (XPS) spectrum of 2DAHs Ag/a-WO_{3-x} confirms the composition of W, O, and Ag elements totally (Fig. S8). The binding energies of W 4f and O 1s in Ag/a-WO_{3-x} shown in Fig. 2b and c are negatively shifted by ca. 0.23 eV and 0.48 eV, respectively, as compared to those for a-WO_{3-x}. The deconvoluted high-resolution XPS of selected core energy level peak regions of O 1s for these samples are shown in Fig. S9, and the relevant components of these species obtained from the relative peak area are presented in Table S1. Here, we also mentioned that the introduced Ag nanoparticles on a-WO_{3-x} can induce the reduction of oxygen defects to some degree. Moreover, the binding energy of Ag 3d in Ag/a-WO_{3-x} is positively shifted by ca. 0.20 eV compared to that of Ag nanoparticles (Fig. 2d), which confirms that the electrons transfer from Ag to a-WO_{3-x} [37]. The Ag 3d_{5/2} and Ag 3d_{3/2} peaks at the binding energy of 368.1 eV and 374.1 eV for Ag/a-WO_{3-x} are good fits for Ag⁰ 4f peaks

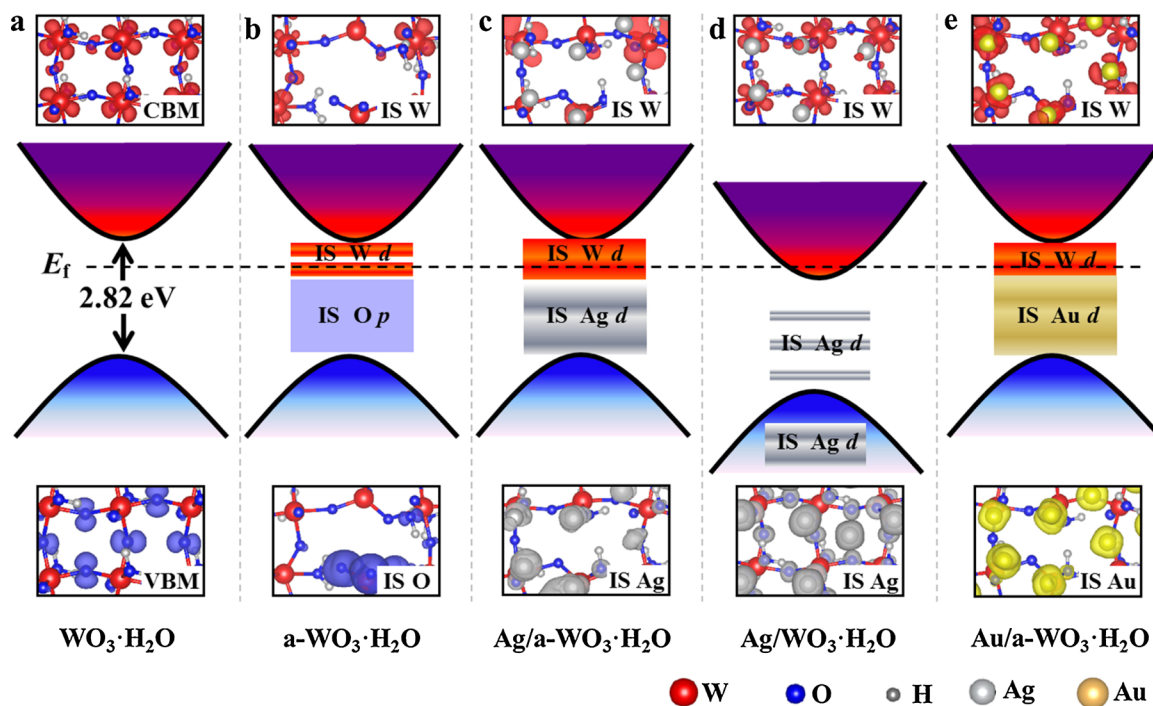


Fig. 5. Schematic of calculated position and the shifting trend of interface state (IS) in the gap of (a) $\text{WO}_3 \cdot \text{H}_2\text{O}$, (b) $\text{a-WO}_3 \cdot \text{H}_2\text{O}$, (c) $\text{Ag/a-WO}_3 \cdot \text{H}_2\text{O}$, (d) $\text{Ag/WO}_3 \cdot \text{H}_2\text{O}$ and (e) $\text{Au/a-WO}_3 \cdot \text{H}_2\text{O}$. The narrow and broad red (gray) bars represent localized and relatively delocalized IS W-d (Ag-d) state, respectively. The blue bar represents IS O-p state. The yellow bar represents relatively delocalized IS Au-d state. The partial charge density of IS are also plotted to show the properties of different IS (top and bottom). The Fermi level is marked by black dotted line and all the systems are aligned with Fermi level (For interpretation of the references to colour in this figure legend, the reader is referred to the web version of this article).

[38]. In all, the results above confirm that 2DAHs Ag/a-WO_{3-x} have been obtained successfully.

3.3. Synergistic photocatalysis effect of 2DAHs of Ag/a-WO_{3-x}

Considering the specific structure of 2DAHs Ag/a-WO_{3-x} combines both strongly LSPR of Ag and amorphous effect of a-WO_{3-x} , it is naturally to explore the photocatalytic efficiency. It is well-known that the photocatalytic efficiency is highly related to the light absorption, then the UV–vis absorption spectra of Ag/a-WO_{3-x} , a-WO_{3-x} and Ag nanoparticles are tested and plotted in Fig. 3a. For pure Ag nanoparticles, they have typical characteristic absorption peaks, while for Ag/a-WO_{3-x} , the disappearance of characteristic peaks suggests that there is no metal aggregation. The more fascinating phenomenon is that there is strong photon absorption in the entire UV–vis region for both Ag/a-WO_{3-x} and a-WO_{3-x} , moreover the strength of photon absorption in Ag/a-WO_{3-x} is much stronger than that of a-WO_{3-x} . This phenomenon can be further proved in theoretical calculations as presented in Fig. 3b. And it shows that there is almost no optical gap in Ag/a-WO_{3-x} , but a small optical gap in a-WO_{3-x} . It means that Ag/a-WO_{3-x} can utilize broad spectrum of light for photoelectrochemical (PEC) catalysis.

A standard three-electrode PEC cell was set up to test the optoelectronic conversion performance of the 2DAHs of Ag/a-WO_{3-x} . LSV curves of Ag/a-WO_{3-x} and a-WO_{3-x} electrodes under illumination (AM1.5 G , 100 mW cm^{-2}) were obtained to compare the catalytic nature of these electrodes for evaluating their optoelectronic conversion performance. Fig. S10 shows that the Ag/a-WO_{3-x} heterostructures shifts the onset potential for O_2 evolution to the positive direction by approximately 200 mV. The photocurrent responses of the PEC devices are recorded for several ON-OFF cycles under simulated solar light illumination (Fig. 4a). For Ag/a-WO_{3-x} , its photocurrent response is about 2.6 times higher than that of a-WO_{3-x} , while the latter only attributes to the amorphous effect. Compared to Ag/WO_3 , the photocurrent response of Ag/a-WO_{3-x} is about 1.7 times higher than that of it,

because Ag/WO_3 just owing to the LSPR effect. Electrochemical impedance spectroscopy (EIS) has been used to investigate the kinetics of the PEC processes occurring at electrode/electrolyte interfaces (Fig. 4b) [39,40]. It can be seen that the representative Nyquist plots display an obviously decreased charge transfer resistance (R_{ct}) for Ag/a-WO_{3-x} compared to both a-WO_{3-x} and Ag/WO_3 systems. These results indicate that the 2DAHs Ag/a-WO_{3-x} can suppress the recombination of photo-generated electrons and holes efficiently [31,37]. Moreover, the experimental result of Ag/a-WO_{3-x} photoanode at a constant bias of 0.8 V vs. Ag/AgCl under AM 1.5 G simulated sunlight for 180 min demonstrates that it has long term sustainability (Fig. S11).

To properly evaluate the PEC efficiency, we conducted the incident photo-to-current conversion efficiency (IPCE) measurements at a bias potential of 0.8 V vs Ag/AgCl from 360 to 650 nm (Fig. 4c). We find that Ag/a-WO_{3-x} shows much higher IPCE than that of a-WO_{3-x} , which is well-matched with their corresponding absorption peaks in the visible region. Traditionally, the improved photocatalysis activity can be explained due to the LSPR effect [41–43]. However, from our experimental results shown in Fig. 4a, the photocurrent value of Ag/a-WO_{3-x} is much higher than that of a-WO_{3-x} and Ag/WO_3 , respectively. It indicates that besides LSPR effect, additional underlying effect plays essential role in Ag/a-WO_{3-x} . This inspires us to explore what dramatically enhances the PEC performance.

Besides to the PEC measurements of Ag/a-WO_{3-x} , we also test the sample of Au/a-WO_{3-x} heterostructures in order to extend the 2DAHs systems for high-efficiency catalysis (Fig. S12–Fig. S19). We find that both the 2DAHs systems can be used for the PEC water splitting. However, the PEC water splitting OER activity of Ag/a-WO_{3-x} is slightly higher than that of Au/a-WO_{3-x} , which is due to the standard potential level of water oxidation is quite different (Fig. 4d). Thanks to the higher IS W-d state of Au, the energy difference of 5.48 eV between the position of IS d state (W-d and Au-d) and the vacuum level is less than the standard potential level of water oxidation 5.67 eV [44,45]. On the contrary, in Ag/a-WO_{3-x} , it is 6.02 eV that is slightly greater than the

standard potential level of water oxidation owing to the lower position of IS *d* state. While in crystalline WO₃, due to the much lower position of VBM, the calculated 7.24 eV is much greater than the standard potential level of water oxidation. Taken together, we conclude that the PEC water splitting OER activity is more facilitated in the system of Ag/a-WO_{3-x}.

To explain the above experimental phenomena that PEC activity of Ag/a-WO_{3-x} is superior to that of a-WO_{3-x}, Ag/WO₃ and Au/a-WO_{3-x}, we carried out the DFT calculations to investigate the electronic structures of the involved systems [46,47]. The constructed calculated models and DOS of different case of structures are presented in Fig. S20–Fig. S23. Fig. 5 presents the energy levels of IS in the gap of WO₃, a-WO_{3-x}, Ag/a-WO_{3-x}, Ag/WO₃ and Au/a-WO_{3-x} systems, respectively. Compared with the case of WO₃ in Fig. 5a, a-WO_{3-x} (see Fig. 5b) clearly shows that the gap of a-WO_{3-x} reduces substantially. The reduced gap of a-WO_{3-x} indicates that after the amorphization process, there are a few IS emerging in the gap of crystalline WO₃, and these IS originate from the valence band maximum (VBM) O-*p* state up shift and conduction band minimum (CBM) W-*d* state down shift. The underlying mechanism of IS shifting behavior is attributed to the O vacancy-induced enhanced random bonding between loaded Ag atoms and substrate atoms. Although IS O-*p* state is delocalized, the electronic occupation states is quite small. This naturally leads to the relatively easy electrons transition from the occupied IS O-*p* state to unoccupied IS W-*d* state, but in the electrons transition process, the probability is relatively less because of *p-d* coupling. In sharp contrast, for the Ag/a-WO_{3-x}, the probability of photon transition is much more than that of a-WO_{3-x}. This is caused by the fact that Ag loading on a-WO_{3-x} not only shifts down the *d* state of W atom from the conduction band to the gap (formed tail states) [48], which in turn induces the IS W-*d* state to become relatively delocalized compared with the case of a-WO_{3-x}, but also moves up the *d* state of Ag atom from the valence band to the gap as seen in Fig. 5c. Since the completely distorted amorphous structure of Ag/a-WO_{3-x} and as well as spin-orbit coupling [49], the coupling of *d-d* tail states becomes much stronger, resulting in the permission of the *d*(W)-*d*(Ag) transition with high probability. This is quite different from the case of Ag on the WO₃ with O-vacancies (Fig. S24), and the above *d-d* transition is forbidden because of only the localized defect *d* states of W in the gap.

Finally, we compare the Ag/WO₃ with Ag/a-WO_{3-x} to explore the role of crystalline and amorphous heterostructures. Fig. 5d shows the electronic properties of Ag/WO₃, we find only a few localized Ag-*d* states in the gap with the *d-d* transition forbidden. Such PEC activity is mainly related to LSPR effect which have been reported in the literature [50,51]. Thus, the PEC activity of Ag/a-WO_{3-x} system is a synergistic effect of both amorphous effect and LSPR effect, which are derived from a-WO_{3-x} and Ag nanoparticles individually. Additionally, we also noticed that the same synergistic effect can be found in the Au/a-WO_{3-x} system, as shown the calculation results in Fig. 5e. However, because of the strong relativistic effect and relatively more delocalized *d* band of Au, *d-d* tail states coupling is relatively weaker than that of Ag/a-WO_{3-x}, resulting relatively weaker PEC performance. Therefore, Ag/a-WO_{3-x} system is advantageous over Au/a-WO_{3-x} because the synergistic effect needs not only from different transition metals, but also requires the adequate position of different *d* states.

4. Conclusions

In summary, based on the building of 2D amorphous WO_{3-x} with assistance of SC CO₂, a well-defined 2D amorphous heterostructures system of Ag/a-WO_{3-x} is successfully realized. Further OER photocatalysis studies indicate that those Ag(Au)/a-WO_{3-x} systems have been dramatically improved compared to single a-WO_{3-x} or Ag/WO₃ systems, and DFT calculations demonstrate the enhanced PEC performance attributes to the superposition effect of both amorphous effect catalysis and LSPR catalysis. The underlying physical mechanism of the

amorphous effect catalysis stems from the unique *d-d* tail states coupling of Ag and W atoms. Overall, our new findings will open a new approach for the development of new materials system for high-efficiency catalyst performance.

Acknowledgements

This work is supported partly by the National Natural Science Foundation of China (No. 21773216, 51173170, 21571157, 11304288, 11774078), and partly by the financial support from the Innovation Talents Award of Henan Province (114200510019).

Appendix A. Supplementary data

Supplementary material related to this article can be found, in the online version, at doi:<https://doi.org/10.1016/j.apcatb.2019.01.015>.

References

- [1] K.S. Novoselov, A. Mishchenko, A. Carvalho, A.H. Castro Neto, 2D materials and van der Waals heterostructures, *Science* 353 (2016) aac9439.
- [2] Q.H. Wang, K. Kalantar-Zadeh, A. Kis, J.N. Coleman, M.S. Strano, Electronics and optoelectronics of two-dimensional transition metal dichalcogenides, *Nat. Nanotechnol.* 7 (2012) 699–712.
- [3] H. Zhang, Ultrathin two-dimensional nanomaterials, *ACS Nano* 9 (2015) 9451–9469.
- [4] N.R. Wilson, P.V. Nguyen, K. Seyler, P. Rivera, A.J. Marsden, Z.P.L. Laker, G.C. Constantinescu, V. Kandyba, A. Barinov, N.D.M. Hine, X.D. Xu, D.H. Cobden, Determination of band offsets, hybridization, and exciton binding in 2D semiconductor heterostructures, *Sci. Adv.* 3 (2017) e1601832.
- [5] D. Jariwala, T.J. Marks, M.C. Hersam, Mixed-dimensional van der Waals heterostructures, *Nat. Mater.* 16 (2017) 170–181.
- [6] Y.T. Lee, P.J. Jeon, J.H. Han, J. Ahn, H.S. Lee, J.Y. Lim, W.K. Choi, J.D. Song, M.C. Park, S. Im, D.K. Hwang, Mixed-dimensional 1D ZnO-2D WSe₂ van der Waals heterojunction device for photosensors, *Adv. Funct. Mater.* 27 (2017) 1703822.
- [7] H.L. Wu, Z. Kang, Z.H. Zhang, Z. Zhang, H.N. Si, Q.L. Liao, S.C. Zhang, J. Wu, X.K. Zhang, Y. Zhang, Interfacial charge behavior modulation in perovskite quantum dot-monolayer MoS₂ 0D-2D mixed-dimensional van der Waals heterostructures, *Adv. Funct. Mater.* (2018) 1802015.
- [8] S. Liu, Q.L. Liao, Z. Zhang, X.K. Zhang, S.N. Lu, L.X. Zhou, M.Y. Hong, Z. Kang, Y. Zhang, Strain modulation on graphene/ZnO nanowire mixed-dimensional van der Waals heterostructure for high-performance photosensor, *Nano Res.* 10 (2017) 3476–3485.
- [9] Y.M. Ren, Q. Xu, C.Z. Wang, X.L. Zheng, Y. Jia, Y.H. Qi, Y.C. Zhou, X.A. Yang, Z.Y. Zhang, CO₂-assisted solution-phase selective assembly of 2D WS₂-WO₃·H₂O and 1T-2H MoS₂ to desirable complex heterostructures, *ChemNanoMat* 9 (2017) 632–638.
- [10] Z.Y. Cai, B.L. Liu, X.L. Zou, H.M. Cheng, Chemical vapor deposition growth and applications of two-dimensional materials and their heterostructures, *Chem. Rev.* 118 (2018) 6091–6133.
- [11] L. Liu, J. Park, D.A. Siegel, K.F. McCarty, K.W. Clark, W. Deng, L. Basile, J.C. Idrobo, A.P. Li, G. Gu, Heteroepitaxial growth of two-dimensional hexagonal boron nitride templated by graphene edges, *Science* 343 (2014) 163–167.
- [12] Y.J. Gong, J.H. Lin, X.L. Wang, G. Shi, S.D. Lei, Z. Lin, X.L. Zou, G.L. Ye, R. Vajtai, B.I. Yakobson, H. Terrones, M. Terrones, B.K. Tay, J. Lou, S.T. Pantelides, Z. Liu, W. Zhou, P.M. Ajayan, Vertical and in-plane heterostructures from WS₂/MoS₂ monolayers, *Nat. Mater.* 13 (2014) 1135–1142.
- [13] X.D. Duan, C. Wang, J.C. Shaw, R. Cheng, Y. Chen, H.L. Li, X.P. Wu, Y. Tang, Q.L. Zhang, A.L. Pan, J.H. Jiang, R.Q. Yu, Y. Huang, X.F. Duan, Lateral epitaxial growth of two-dimensional layered semiconductor heterojunctions, *Nat. Nanotechnol.* 9 (2014) 1024–1030.
- [14] X. Zhang, Z.M. Luo, P. Yu, Y.Q. Cai, Y.H. Du, D.X. Wu, S. Gao, C.L. Tan, Z. Li, M.Q. Ren, T. Osipowicz, S.M. Chen, Z. Jiang, J. Li, Y. Huang, J. Yang, Y. Chen, C.Y. Ang, Y.L. Zhao, P. Wang, L. Song, X.J. Wu, Z. Liu, A. Borgna, H. Zhang, Lithiation-induced amorphization of Pd₃P₂S₈ for highly efficient hydrogen evolution, *Nat. Catal.* 1 (2018) 460–468.
- [15] J.Y. Shi, Y. Kuwahara, M.C. Wen, M. Navlani-Garcia, K. Mori, T.C. An, H. Yamashita, Room-temperature and aqueous-phase synthesis of plasmonic molybdenum oxide nanoparticles for visible-light-enhanced hydrogen generation, *Chem. Asian J.* 11 (2016) 2377–2381.
- [16] X.T. Wang, W.X. Shi, Z. Jin, W.F. Huang, J. Lin, G.S. Ma, S.Z. Li, L. Guo, Remarkable SERS activity observed from amorphous ZnO nanocages, *Angew. Chem. Int. Ed.* 56 (2017) 9851–9855.
- [17] P. Zhou, J.P. Lai, Y.H. Tang, Y.G. Chao, F. Lin, S.J. Guo, Amorphous FeCoPO_x nanowires coupled to g-C₃N₄ nanosheets with enhanced interfacial electronic transfer for boosting photocatalytic hydrogen production, *Appl. Catal. B-Environ* 238 (2018) 161–167.
- [18] X.H. Meng, D. Deng, Trash to treasure: waste eggshells as chemical reactors for the synthesis of amorphous Co(OH)₂ nanorod arrays on various substrates for applications in rechargeable alkaline batteries and electrocatalysis, *ACS Appl. Mater.*

- Interfaces 9 (2017) 5244–5253.
- [19] Y.Y. Kang, Y.Q. Yang, L.C. Yin, X.D. Kang, G. Liu, H.M. Cheng, An amorphous carbon nitride photocatalyst with greatly extended visible-light-responsive range for photocatalytic hydrogen generation, *Adv. Mater.* 27 (2015) 4572–4577.
- [20] P.D. Tran, T.V. Tran, M. Orio, S. Torelli, Q.D. Truong, K. Nayuki, Y. Sasaki, S.Y. Chiam, R. Yi, I. Honma, J. Barber, V. Artero, Coordination polymer structure and revisited hydrogen evolution catalytic mechanism for amorphous molybdenum sulfide, *Nat. Mater.* 15 (2016) 640–646.
- [21] C.G. Morales-Guio, X.L. Hu, Amorphous molybdenum sulfides as hydrogen evolution catalysts, *Acc. Chem. Res.* 47 (2014) 2671–2681.
- [22] W. Liu, Q. Xu, W.L. Cui, C.H. Zhu, Y.H. Qi, CO₂-assisted fabrication of two-dimensional amorphous molybdenum oxide nanosheets for enhanced plasmon resonances, *Angew. Chem. Int. Ed.* 56 (2017) 1600–1604.
- [23] (a) J. Heyd, G.E. Scuseria, M. Ernzerhof, Hybrid functionals based on a screened coulomb potential, *J. Chem. Phys.* 118 (2003) 8207–8215; (b) J. Heyd, G.E. Scuseria, M. Ernzerhof, Erratum: “Hybrid functionals based on a screened coulomb potential”, [*J. Chem. Phys.* 118 (2003) 8207–8215.], *J. Chem. Phys.* 124 (2006) 219906.
- [24] G. Kresse, Efficient iterative schemes for *ab initio* total-energy calculations using a plane-wave basis set, *Phys. Rev. B* 54 (1996) 11169–11186.
- [25] P.E. Blöchl, Projector augmented-wave method, *Phys. Rev. B* 50 (1994) 17953–17979.
- [26] Y.M. Ren, C.Z. Wang, Y.H. Qi, Z.M. Chen, Y. Jia, Q. Xu, CO₂-induced defect engineering: a new protocol by doping vacancies in 2D heterostructures for enhanced visible-light photocatalysis, *Appl. Surf. Sci.* 149 (2017) 573–579.
- [27] N. Wang, Q. Xu, S.S. Xu, Y.H. Qi, M. Chen, H.X. Li, B.X. Han, High-efficiency exfoliation of layered materials into 2D nanosheets in switchable CO₂/surfactant/H₂O system, *Sci. Rep.* 5 (2015) 16764.
- [28] Y.H. Qi, N. Wang, Q. Xu, H.X. Li, P.S. Zhou, X. Lu, G.Q. Zhao, A green route to fabricate MoS₂ nanosheets in water-ethanol-CO₂, *Chem. Commun. (Camb.)* 51 (2015) 6726–6729.
- [29] A.D. Paola, L. Palmisano, A.M. Venezia, V. Augugliaro, Coupled semiconductor systems for photocatalysis. Preparation and characterization of polycrystalline mixed WO₃/WS₂ powders, *J. Phys. Chem. B* 103 (1999) 8236–8244.
- [30] P.S. Zhou, Q. Xu, H.X. Li, Y. Wang, B. Yan, Y.C. Zhou, J.F. Chen, J.N. Zhang, K.X. Wang, Fabrication of two-dimensional lateral heterostructures of WS₂/WO₃·H₂O through selective oxidation of monolayer WS₂, *Angew. Chem. Int. Ed.* 54 (2015) 15226–15230.
- [31] Y.M. Ren, Q. Xu, X.L. Zheng, Y.Z. Fu, Z. Wang, H.L. Chen, Y.X. Weng, Y.C. Zhou, Building of peculiar heterostructure of Ag/two-dimensional fullerene shell-WO_{3-x} for enhanced photoelectrochemical performance, *Appl. Catal. B-Environ* 231 (2018) 381–390.
- [32] Y.H. Sang, Z.H. Zhao, M.W. Zhao, P. Hao, Y.H. Leng, H. Liu, From UV to near-infrared, WS₂ nanosheet: a novel photocatalyst for full solar light spectrum photodegradation, *Adv. Mater.* 27 (2015) 363–369.
- [33] F.C. Lei, Y.F. Sun, K.T. Liu, S. Gao, L. Liang, B.C. Pan, Y. Xie, Oxygen vacancies confined in ultrathin indium oxide porous sheets for promoted visible-light water splitting, *J. Am. Chem. Soc.* 136 (2014) 6826–6829.
- [34] M.S. Zhu, P.L. Chen, M.H. Liu, Sunlight-driven plasmonic photocatalysts based on Ag/AgCl nanostructures synthesized via an oil-in-water medium: enhanced catalytic performance by morphology selection, *J. Mater. Chem.* 21 (2011) 16413–16419.
- [35] J. Huang, D.Y. Ma, F. Chen, D.Z. Chen, M. Bai, K.W. Xu, Y.X. Zhao, Green in situ synthesis of clean 3D chestnutlike Ag/WO_{3-x} nanostructures for highly efficient, recyclable and sensitive SERS sensing, *ACS Appl. Mater. Interfaces* 9 (2017) 7436–7446.
- [36] G.C. Xi, J.H. Ye, Q. Ma, N. Su, H. Bai, C. Wang, In situ growth of metal particles on 3D urchin-like WO₃ nanostructures, *J. Am. Chem. Soc.* 134 (2012) 6508–6511.
- [37] Y. Shi, J. Wang, C. Wang, T.T. Zhai, W.J. Bao, J.J. Xu, X.H. Xia, H.Y. Chen, Hot electron of Au nanorods activates the electrocatalysis of hydrogen evolution on MoS₂ nanosheets, *J. Am. Chem. Soc.* 137 (2015) 7365–7370.
- [38] H.F. Cheng, B.B. Huang, P. Wang, Z.Y. Wang, Z.Z. Lou, J.P. Wang, X.Y. Qin, X.Y. Zhang, Y. Dai, In situ ion exchange synthesis of the novel Ag/AgBr/BiOBr hybrid with highly efficient decontamination of pollutants, *Chem. Commun. (Camb.)* 47 (2011) 7054–7056.
- [39] Q. Wang, J.E. Moser, M. Gratzel, Electrochemical impedance spectroscopic analysis of dye-sensitized solar cells, *J. Phys. Chem. B* 109 (2005) 14945–14953.
- [40] Q.C. Zhuang, T. Wei, L.L. Du, Y.L. Cui, L. Fang, S.G. Sun, An electrochemical impedance spectroscopic study of the electronic and ionic transport properties of spinel LiMn₂O₄, *J. Phys. Chem. C* 114 (2010) 8614–8621.
- [41] N.Q. Wu, Plasmonic metal-semiconductor photocatalysts and photoelectrochemical cells: a review, *Nanoscale* 10 (2018) 2679–2696.
- [42] Y.C. Zhang, S. He, W.X. Guo, Y. Hu, J.W. Huang, J.R. Mulcahy, W.D. Wei, Surface-plasmon-driven hot electron photochemistry, *Chem. Rev.* 118 (2018) 2927–2954.
- [43] C. Clavero, Plasmon-induced hot-electron generation at nanoparticle/metal-oxide interfaces for photovoltaic and photocatalytic devices, *Nat. photon.* 8 (2014) 95–103.
- [44] V. Chakrapani, J.C. Angus, A.B. Anderson, S.D. Wolter, B.R. Stoner, G.U. Sumanasekera, Charge transfer equilibria between diamond and an aqueous oxygen electrochemical redox couple, *Science* 318 (2007) 1424–1430.
- [45] H.L. Zhuang, R.G. Hennig, Single-layer group-III monochalcogenide photocatalysts for water splitting, *Chem. Mater.* 25 (2013) 3232–3238.
- [46] G. Hollinger, T.M. Duc, A. Deneuve, Charge transfer in amorphous colored WO₃ films observed by X-ray photoelectron spectroscopy, *Phys. Rev. Lett.* 37 (1976) 1564–1567.
- [47] J.W. Chiou, S.C. Ray, H.M. Tsai, C.W. Pao, F.Z. Chien, W.F. Pong, C.H. Tseng, J.J. Wu, M.H. Tsai, C.H. Chen, H.J. Lin, J.F. Lee, J.H. Guo, Correlation between electronic structures and photocatalytic activities of nanocrystalline-(Au, Ag, and Pt) particles on the surface of ZnO nanorods, *J. Phys. Chem. C* 115 (2011) 2650–2655.
- [48] P.W. Anderson, Absence of diffusion in certain random lattices, *Phys. Rev.* 109 (1958) 1492–1505.
- [49] C.D. Baertsch, K.T. Komala, Y.H. Chua, E. Iglesia, Genesis of brønsted acid sites during dehydration of 2-Butanol on tungsten oxide catalysts, *J. Catal.* 205 (2002) 44–57.
- [50] S.Y. Wang, Y.Y. Gao, S. Miao, T.F. Liu, L.C. Mu, R.G. Li, F.T. Fan, C. Li, Positioning the water oxidation reaction sites in plasmonic photocatalysts, *J. Am. Chem. Soc.* 139 (2017) 11771–11778.
- [51] D.B. Ingram, S. Linic, Water splitting on composite plasmonic-metal/semiconductor photoelectrodes: evidence for selective plasmon-induced formation of charge carriers near the semiconductor surface, *J. Am. Chem. Soc.* 133 (2011) 5202–5205.